Runback ice formation mechanism on hydrophilic and superhydrophobic surfaces

D. Mangini[1+], C.Antonini[1,2+], M. Marengo[1,3], A. Amirfazli[4*]

[1] Department of Engineering, University of Bergamo, viale Marconi 5, 24044 Dalmine, Italy.

[2] Laboratory of Thermodynamics in Emerging Technologies, Mechanical and Process Engineering Department, ETH Zürich, 8092 Zürich, Switzerland.

[3] School of Computing, Engineering and Mathematics, University of Brighton, Brighton BN2 4GJ, UK

[4] Department of Mechanical Engineering, York University, Toronto, ON, M3J13P, Canada.

+ C. Antonini and D. Mangini contributed equally to this study

* Corresponding author: alidad2@yorku.ca

Keywords: superhydrophobicity, icephobicity, anti-ice coatings, icing mitigation

Abstract

Experimental results aimed at understanding the different mechanisms of ice accretion on surfaces with different wettability is presented. Ice accretion was studied on a hydrophilic and a superhydrophobic surface of NACA 0021 airfoils, during tests inside an icing wind tunnel. Visualization of ice accretion was performed using an infrared camera, which allows an enhanced view of liquid water and ice present on the airfoil surface compared to the optical imaging. The use of the infrared camera permitted identification of different ice shapes and ice formation mechanisms on the test articles: on the hydrophilic sample, a compact ice front accreted, whereas on the superhydrophobic sample, small isolated ice islands formed. In addition, the ice on the superhydrophobic sample was more susceptible to be shed from the surface, as shown by shedding of several ice islands due to aerodynamic drag during tests. Combined analysis of infrared camera images and optical images confirmed that the fraction of the airfoil covered by ice decreases for the superhydrophobic sample, for a two minutes of test, for all the input heat power tested.

1 Introduction

Icing on structures poses considerable risk for safety and has a significant economic impact in many different areas such as aeronautics (Gent et al. 2000), power systems, e.g. wind turbines (Dalili et al. 2007) electric power transmission lines (Farzaneh and Masoud 2008), and structures such as bridges and oil platforms. Current systems to combat icing are typically thermally based, requiring significant supply of hot air or electrical energy, or make use of freezing depressant chemicals, which are expensive and potentially harmful for the environment. In aviation or wind turbine industry, fully evaporative anti-icing systems often need to be implemented to avoid ice accretion in critical areas, e.g. close to flow stagnation point, such as on wing or nacelle leading edges, where drop collection is the highest, and also to avoid ice accretion downstream, where anti-icing systems are not present and runback water can freeze. However, this approach requires a large amount of energy to be spent on evaporation of liquid water on the surface. For these reasons, in recent years there has been an intense interest in the so called superhydrophobic and icephobic surfaces, which have a great potential to combat ice accretion, due to their ability to repel water and ice, respectively (Bahadur et al. 2011, Cao et al. 2009, Eberle et al. 2014, Jung et al. 2011, Kulinich et al. 2009, Meuler et al. 2010a, Meuler et al. 2010b, Shirtcliffe et al. 2010, Tarquini et al. 2014, Tourkine et al.2009, Varanasi et al. 2009, Zheng et al. 2011). Typically many surfaces that are susceptible to icing (as discussed in above areas) are hydrophilic. On a hydrophilic surface, i.e. a surface with contact angle, θ, less than 90° (see Fig. 1a), water drops sit fairly flat, which means when a shear flow is present, the aerodynamic drag on the drop can be low. In contrast, for a hydrophobic surface, with θ larger than 90°, the drops tend to bead. For a superhydrophobic surface, where θ is larger than 135° (Rioboo et al. 2012), not only drops takes an almost spherical shape on the surface (see Fig. 1b), but also the capillary adhesion

force, resisting drop mobility, is low, as a result of high contact angle and low contact angle hysteresis, $\Delta\theta$ (defined as the difference between the advancing and receding contact angles) (Pierce et al. 2008). In an earlier work (Milne and Amirfazli 2009), it was shown that combination of low adhesion and high drag force experienced by drops on superhydrophobic surfaces can lead to easy shedding of water drops from such surfaces. Indeed, a combination of drop rebound after impact on superhydrophobic surfaces (Antonini et al. 2013), as well as drop shedding in the presence of a shear flow, can take away drops from a surface, reducing water accumulation on it and thus can prevent or limit ice accretion. These mechanisms of water removal were used to explain the reduction in icing (especially of runback type) on airfoils, when they are made of superhydrophobic compared to hydrophilic airfoils (see Antonini et al. 2011). However, a direct observation of ice accretion on surfaces of different wettability, needed to provide a more complete explanation of icing mechanism, is still missing. Understanding the icing mechanism is especially important for runback ice as superhydrophobic surfaces have seen to be very effective in reduction of this type of icing (Antonini et al. 2011). As such, the focus of this study is an exploring the physical phenomena of icing and not a particular application area.

2 Experimental setup

2.1 Icing wind tunnel

Experiments were conducted in an open loop wind tunnel (Fig. 2), which had a rectangular test cross section of 254x305 mm and a length of 305 mm. The air velocity in the test section was 14.4 m/s, corresponding to an air volumetric flow of 1.15 m^3/s. The test section was made of transparent acrylic to allow visually observation of the samples from all directions. To obtain icing conditions, the tunnel was placed inside a cold room, where the static air

temperature was kept constant at -17°C. The liquid water cloud was generated using two different nozzle spray systems, for generating two different icing conditions: in the first condition, referred to as "*disperse spray*", the MVD was 50 µm and LWC was 2.5 g/m^3, which corresponds to very severe icing conditions, according to FAR29, Appendix C; in the second condition, referred to as "*dense spray*", MVD was 125 µm and LWC was 6.5 g/m^3. For a more complete technical description of the set-up, see Antonini et al. 2011 (note that the airspeed was set differently in this study). Icing test duration was two minutes. A A320 FLIR® infrared (IR) camera with a 10mm/45° lens was fixed above the airfoil leading edge. The IR camera and ThermoVision® ExaminIR™ software were used for thermal imaging of ice accretion on the airfoil surface during the test, through an IR window installed in the test section. The IR window was protected from icing by a thin warm air layer blown over the inside surface of the window (Mohseni et al. 2012). Imaging was performed at 2 fps (frames per second) with a typical resolution of 29 pixel/cm, and images were stored in a computer for post-processing. The main reason to use an IR camera, rather than an optical camera, was the improvement of contrast between the solid substrate against liquid water and ice, taking advantage of the different emissivity. Also, liquid water and ice, despite having similar emissivity coefficient of 0.97 and 0.98, respectively, could be differentiated looking at image sequences: e.g., from videos, liquid water was identified since it moved downstream due to shear forces, whereas ice remained attached to the sample at the same position.

2.2 Test article

The test article was a NACA 0021 symmetric airfoil that was placed with a zero angle of attack in the test section. The test article consisted of two components: the main body for the airfoil and an exchangeable insert. These two parts were designed to match geometrically: the central part of the main body (149x305 mm) allowed insertion of the sample to be tested

(79x150 mm, i.e. 53% of wing chord and 49% of wing span). The insert represented the exchangeable section and was made of 6061 T6 aluminum sheet, which was either used as is, or was treated (see the next section) to become superhydrophobic. To simulate the presence of an anti-icing/de-icing heating system, the insert was instrumented with an electrical heater, positioned at the leading edge inside the cavity of airfoil, with a total axial length of 80 mm (the heater axis was parallel to the leading edge, see Fig. 3) . As such, a chord-wise temperature gradient on the airfoil was achieved, as seen for example in aircraft wings. The power consumption was recorded using an electronic oscilloscope (*Tektronix 410A)*.

2.3 Coating of exchangeable inserts

Two different inserts were prepared: (i) untreated bare aluminum, which is hydrophilic, and (ii) a coated aluminum airfoil, with superhydrophobic properties (labeled SHS). Wettability of both surfaces was characterized by measuring advancing and receding contact angles, and their difference, the contact angle hysteresis; values are reported in Table 2. Note that the superhydrophobic sample is characterized both by very high contact angles and a very low contact angle hysteresis. The fabrication process of the superhydrophobic samples is a proprietary process.

2.4 Experimental procedure

The test procedure was as follows: (1) the cold room temperature was set to -17 °C; (2) the wind tunnel fan was started; (3) heating system was switched on and enough time was given, until the ambient and the insert temperature reached steady state conditions; (4) the spray system was activated to generate liquid water cloud; (5) test was run for 2 min; (6) both fan

and spray systems were switched off; and finally (7) optical pictures of the sample were taken, to record resultant ice accretion. An IR camera movie was recorded during each test.

Two levels of input heat power were used in the dense spray condition: 30±1.5 W and 18±0.8 W. The tests were repeated three times for every sample type to ensure reproducibility. The test duration of 2 minutes was chosen since this time was sufficient to visualize ice accretion in the icing conditions.

During the image post-processing, the area covered by ice was also measured both from IR camera movies and from final optical image, using Image-J software.

After each test, the superhydrophobic sample was inspected by conducting simple wetting tests, to identify if eventual coating degraded; no signs of degradation were observed.

3 Results and discussions

3.1 IR visualization

The image sequences in Fig. 3 show first of all the ability to visualize ice accretion evolution during tests because of the different water/aluminum emissivity values. The water drops and the ice that accreted on the surface are visible with an orange/yellow color; the surface appeared violet and blue (except the heated leading edge, visible in a white/yellow color). Since the emissivity values of water and ice are similar, the supplementary videos SV1 and SV2 are also available to understand where ice formed and remained attached to the surface, and where the water was flowing or accumulating on the surface. A representative image sequence of IR camera records is shown in Fig. 3, for the case of dense spray, using 30 W of input heat power. Images for both the hydrophilic (left column) and the superhydrophobic sample (right column) are given, for comparison. On the hydrophilic sample, runback ice formed as a compact front in the unheated area; on the superhydrophobic surface, ice islands

on isolated points were observed (see also Fig. 4 and 6).

The typical mechanism of ice accretion on a hydrophilic sample can be observed with more details in Fig. 4; this figure shows an image at 90 s after start of the spray clouds, different zones are identified. At the heated leading edge, where drop collection was the highest, impinging drop formed a liquid film. While flowing downstream, towards the trailing edge, (from top to bottom in Figure 4), and liquid ligaments (see also video in supplementary information) were observed as the liquid film broke up into fingers. Liquid drops moved downstream due to aerodynamic forces, but did not shed. Finally, the liquid water reached the area away from the heated leading edge so that liquid water froze and runback ice accretion was observed. The ice accreted in the form of a compact front of runback ice on the unheated part of the sample; this resulted in iced area to adhere to the surface, and not shed easily. Thus, ice on the hydrophilic sample continued to accumulate during the test, (Fig. 5 showing time evolution of the area covered by ice visible from the IR camera window). After only 10 s from start of the cloud, the coverage was 20% of the total area visible from the IR camera window, and after two minutes test, the ice covered area was almost the 60%.

On the superhydrophobic surface, the ice accretion mechanism was significantly different. Figure 6a shows a close up view of ice accretion on the superhydrophobic sample for dense spray conditions 50 s after start of the cloud. Instead of ice accretion as a compact front, isolated ice islands can be observed. Ice started to nucleate (Fig. 6b) and grew from isolated points (Fig. 6 c, d, e), forming ice islands that grew during tests, likely due to direct impact of incoming drops.

The visual observation of the runback ice pointed out that the formation of isolated islands seems also beneficial for ice shedding from the sample. It was observed that some ice islands were shed away from the superhydrophobic surface during the tests. Image sequence in Fig.7 shows a sudden detachment of an ice island at time 100 s after the experiment

started. Furthermore, five ice islands were randomly chosen and their area was monitored as function of time (Fig. 8). It can be observed from Fig. 8 that the total ice island area was not increased monotonically during the test, due to ice shedding: three out of five islands were shed from the sample and another one partially detached, while the test was running. A combination of three factors can explain the detachment of the ice. The first factor is the lower area of the ice which is in contact with such surface. The second one is the drag force exerted on the ice islands, because of their different shape compared to the one on the hydrophilic surface: isolated ice islands are protruded from the surface with a high frontal area exposed to the airflow, hence experiencing a higher drag force compared to a flatter ice on the hydrophilic surface. The third factor is the possibility of lower strength of ice adhesion force on surfaces with low wettability (Meuler et al. 2010a). All these factors, taken altogether, facilitate ice shedding from superhydrophobic surfaces.

Finally, it can be noticed that ice accretion is delayed: ice islands started to accrete only from 20s after beginning of the test; after 10 s, the sample is still ice-free (Fig. 9 a).

3.2 Optical images

The area covered by ice at the end of the tests was also calculated by post-processing of the optical images (see Fig. 10). Fig. 10a shows ice accretion on the hydrophilic surface at the end of the test performed with an input heat power of 30 W using the dense spray, and the Fig. 10b the corresponding test on the superhydrophobic surface. The area covered by ice on the hydrophilic surface was 60% of the global area of the sample, while for the superhydrophobic surface it was 20%.

The same mechanisms of ice accretion for both hydrophilic and superhydrophobic surfaces were also observed for disperse spray conditions (see Table 1), as visible in Figure 11.

Additional tests with a heat input of 18 W for both surfaces were performed for the dense

spray condition. Once again, it was observed that on the superhydrophobic surface ice accreted on the sample in the form of ice islands, whereas on the hydrophilic sample in the form of a compact ice front (Fig. 12). Although the input heat power was 40% lower than tests discussed above (i.e. when power was at 30 W), the ice island detachment was still observable during the test (Fig. 13). However, using less heat power, the runback ice on the hydrophilic sample started to accrete closer to the leading edge (Fig. 14) because of the lower temperature along the sample chord. For the superhydrophobic surface, at the end of the test, ice islands were visible closer to the leading edge for the 18 W case, while the other part of the surface remained essentially clean. By post-processing the optical images taken at the end of the tests with heat input of18 W, the area covered by ice was similar with respect the 30W case for both of the surfaces. However, as a result of a reduced heat input on the hydrophilic case the runback ice started to accrete closer to the leading edge; on the superhydrophobic case, ice islands were visible closer to the leading edge (Fig. 14)

4 Summary and conclusions

The present study was aimed at understanding the different mechanisms of ice accretion on surfaces with different wettability, to better understand the potential of a coating strategy against icing on solid surfaces. Ice accretion tests were performed on untreated and treated, i.e. superhydrophobic, aluminum samples inside an open loop icing wing tunnel. By monitoring ice accretion with an IR camera on the different substrates, which were heated at the same power level to simulate an anti-icing system, different ice shapes and ice formation mechanisms could be observed: on the hydrophilic sample, a compact continuous front of ice accreted, whereas on the superhydrophobic sample, small isolated ice islands formed. These results highlight that the surface wettability plays an important role on the ice accretion mechanism.

Three factors can explain the detachment of the ice on superhydrophobic surfaces: the lower area of the ice which is in contact with such surface; the different drag force exerted on the ice islands because of their particular shape with respect to the ice formation on the hydrophilic surface; the lower strength of the adhesion force on surfaces with low wettability.

Finally, the optical images taken at the end of the tests, confirmed a reduction of the area fraction covered by ice for all the heat power level tested ~ 60% for the hydrophilic surface and ~ 20% for the superhydrophobic surface with respect the global area.

All these observed features suggest that a coating strategy based on the use of superhydrophobic surface may be beneficial when used in combination with a thermal anti-icing system to combat ice accretion.

Acknowledgments

The authors acknowledge Regione Lombardia for funding through the project “Strumenti innovativi per il progetto di sistemi antighiaccio per l’aeronautica” (Framework Agreement), and AleniaAermacchi for financial support. The authors are thankful to Fabio Brenna and icing group engineers from AleniaAermacchi for helpful discussions. CA acknowledges funding from a Marie Curie Intra-European Fellowship, within the 7th European Community Framework Programme (ICE^2, 301174). The authors also thank David Barona for superhydrophobic surface preparation.

References

- Antonini, C., Villa, F., Bernagozzi, I. Amirfazli, A., Marengo, M., 2013. Drop Rebound after Impact: The Role of the Receding Contact Angle. Langmuir 29, 16045-16050.
- Antonini, C., Innocenti, M., Horn, T. ,Marengo, M., Amirfazli, A., 2011. Understanding the effect of superhydrophobic coatings on energy reduction in anti-icing systems. Cold Reg. Sci. Techol. 67, 58–67.
- Bahadur, V., Mishchenko, L., Hatton, B.D., Taylor, J.A., Aizenberg, J., Krupenkin, T., 2011. Predictive model for ice formation on superhydrophobic surfaces. Langmuir 23, 14143-14150.
- Cao, L., Jones, A., Sikka, V., Wu, J., and Gao, D., 2009. Anti-icing superhydrophobic coatings. Langmuir 25 (21), 12444-12448.
- Dalili, N., Edrisy, A., Carriveau, R., 2007. A review of surface engineering issues critical to wind turbine performance. Renew Sust. Energ. Rev. 13 (2), 428-438.
- Eberle, P., Tiwari, M.K., Maitra, T., and Poulikakos, D, 2014. The rational nanostructuring of surfaces for extraordinary icephobicity. Nanoscale, 2014, 6, 4874-4881.
- Farzaneh, Masoud, 2008. Atmospheric Icing of Power Networks, Springer, Berlin.
- Gent, R.W., Dart, N.P., Cansdale, J.T., 2000. Aircraft icing. Phil. Trans. R. Soc. London. A 358, 2873-2911.
- Jung, S., Dorrestijn, M., Raps, D., Das, A., Megaridis, C.M., and D. Poulikakos, D., 2011. Are superhydrophobic surfaces best for icephobicity?. Langmuir 27, 3059-3066.
- Kulinich, S.A., Farzaneh, M., 2009. Ice adhesion on superhydrophobic surfaces. Appl. Surf. Sci. 255, 8153-8157.
- Meuler, A.J., Smith, J.D., Varanasi, K.K., Mabry, J.M., McKinley, G.H., Cohen, R.E., 2010a.

Relationship between water wettability and ice adhesion. Appl. Mater. Interfaces 2, 3100-3110.

- Meuler, A.J., McKinley, G.H., Cohen, R.E., 2010b. Exploiting topographical texture to impart icephobicity. ACS Nano 4 (12), 7048–7052.
- Milne, A.J.B., Amirfazli, A., 2009. Drop shedding by shear flow for hydrophilic to superhydrophobic surfaces. Langmuir 25, 14155–14164.
- Mishchenko, L., Hatton, B., Bahadur, V., Taylor, J.A., Krupenkin, T., Aizenberg, J., 2010. Design of Ice-free nanostructured impacting water droplets. ACS Nano 4, 7699-7707.
- Mohseni, M., Amirfazli, A., Frioult, M., 2012. Simultaneous monitoring of ice accretion and thermography o fan airfoil: an IR imaging methodology. Meas. Sci. Technol. 23, 105405.
- Pierce, E., Carmona, F. J., Amirfazli, A, 2008. Understanding of Sliding and Contact Angle Results in Tilted Plate Experiments. Colloid Surface A 323, 73-82.
- Rioboo, R., Delattre, B., Duvivier, D., Vaillant, A., and De Coninck, J., 2012. Superhydrophobicity and liquid repellency of solutions on polypropylene. Adv. Colloid Interface Sci., 175,1−10.
- Shirtcliffe, N. J., McHale, G., Atherton, S., Newton, M. I., 2010. An introduction to superhydrophobicity. Adv. Colloid Interface Sci. 161, 124-138.
- Tarquini, S., Antonini, C., Amirfazli, A., Marengo, M., Palacios, J., 2014. Investigation of ice shedding properties of superhydrophobic coatings on helicopter blades. Cold Reg. Sci. Technol. 100, 50-58.
- Tourkine, P., Le Merrer, M., Quere, D., 2009. Delayed freezing on water repellent materials. Langmuir 25, 7214-7216.
- Varanasi, K. K., Deng, T., Smith, J. D., Hsu, M., Bhate, N., 2010. Frost formation and ice adhesion on superhydrophobic surfaces. Appl. Phys. Lett. 97, 234102.
- Zheng, L., Li, Z., Bourdo, S., Khedir, K.R., Asar, M.R., Ryerson, C.C., Biris, A.S., 2011.

Exceptional superhydrophobicity and low velocity impact icephobicity of Acetone-functionalized carbon nanotube films. Langmuir 27, 9936–9943.

Tables

Table 1. Icing wind tunnel temperature, and icing cloud conditions.

Condition	T[°C]	MVD [µm]	LWC [g/m^3]
dispersed spray	-17	50	2.5
dense spray	-17	125	6.5

Table 2. Wetting properties of different tested samples.

Surface	**θ_A [º]**	**θ_R [º]**	**$\Delta\theta$ [º]**	
Bare aluminum	74±2	10±8	64±10	hydrophilic
SHS	156±3	151±4	5±7	superhydrophobic

Figures

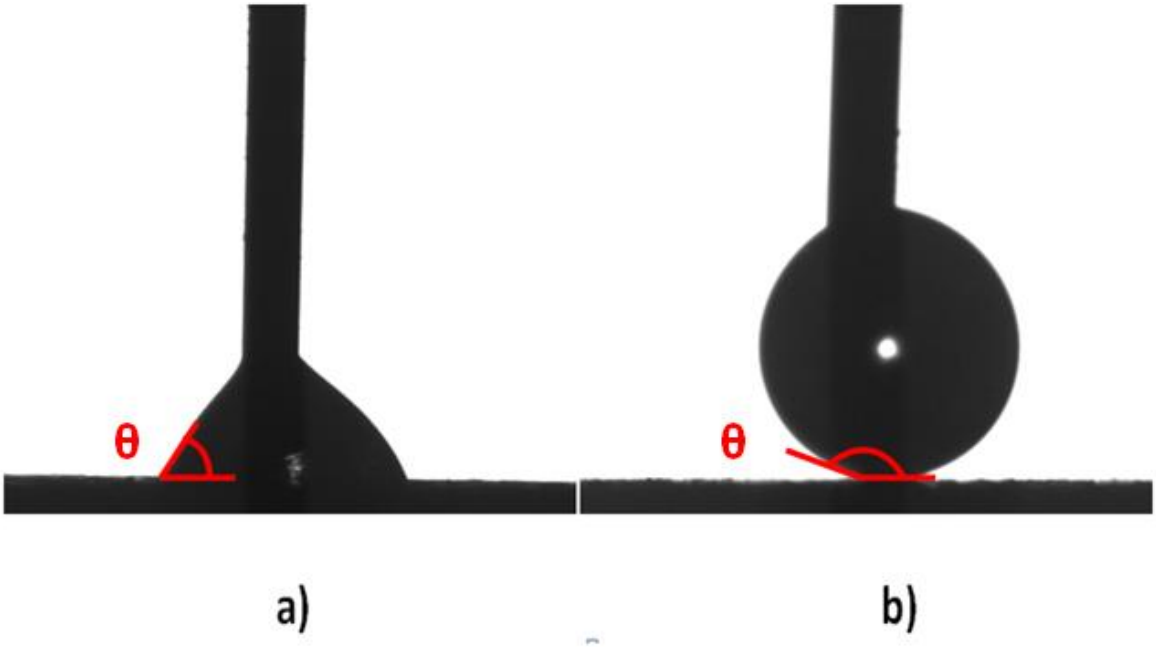

Fig. 1. Sessile water drop on (a) a hydrophilic surface (contact angle, θ, less than 90°) and on (b) a superhydrophobic surface (contact angle, θ, higher than 135°, and low contact angle hysteresis).

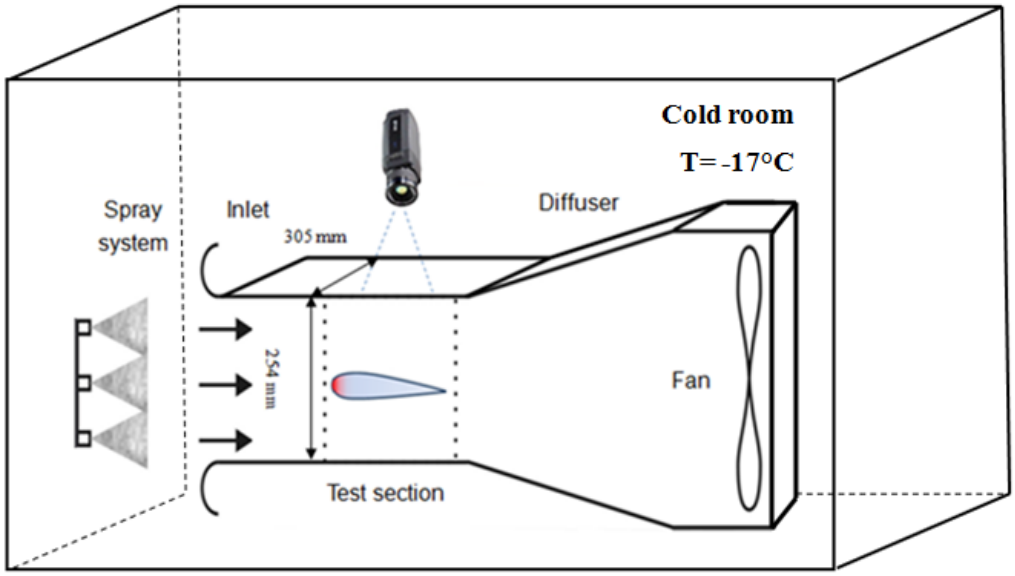

Fig. 2. Schematic of the open-loop icing wind tunnel. The IR camera is mounted above the test

section. The sample was heated on the leading edge to simulate the presence of an anti-icing system.

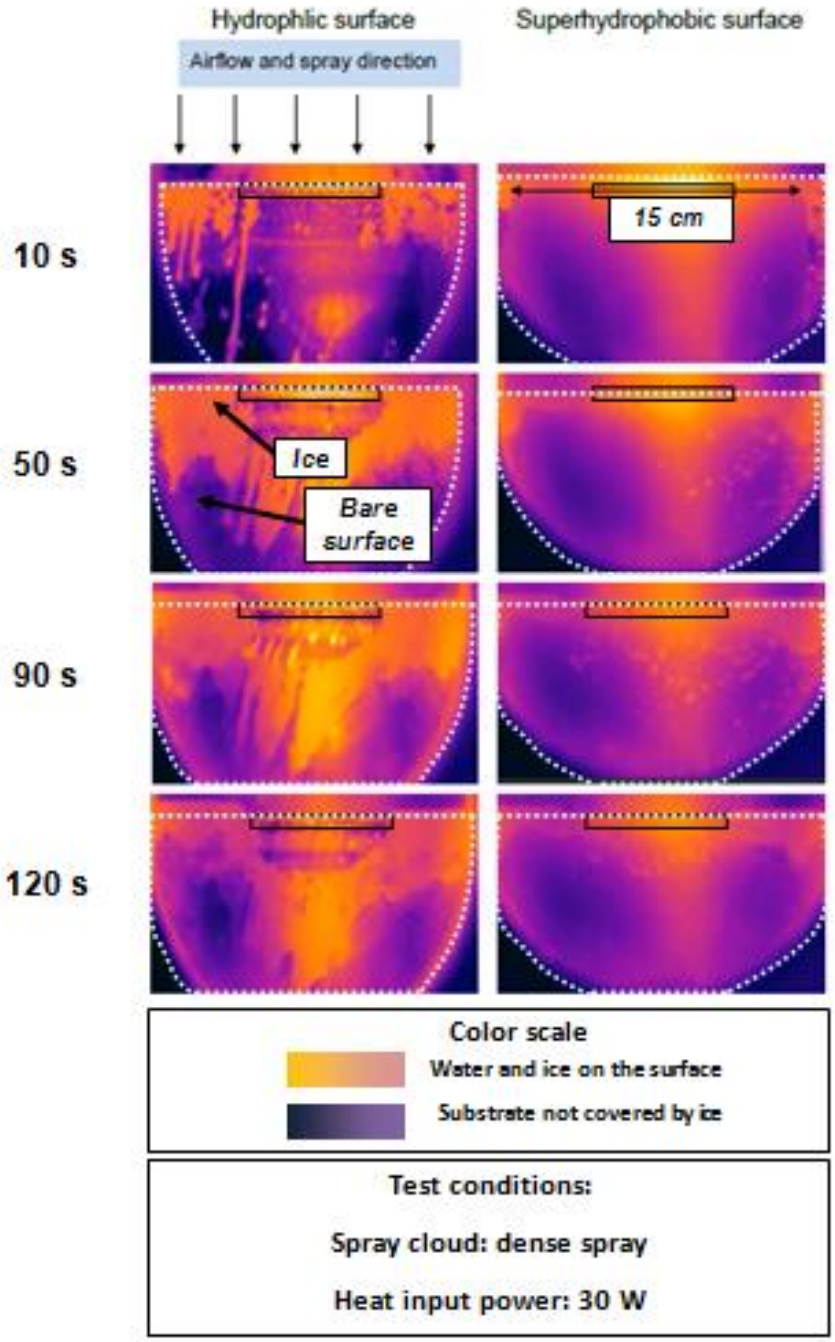

Fig. 3. Top view images for ice accretion on two tested samples using an IR camera: hydrophilic sample (left) and superhydrophobic sample (right). Dotted lines delimit the IR camera window. The black rectangular section shows the position of the heater inside the leading edge of the sample. The water and the ice formed on the surface had a yellow/orange color, while the bare surface blue/violet due to different emissivity (see color image scale and text for details).

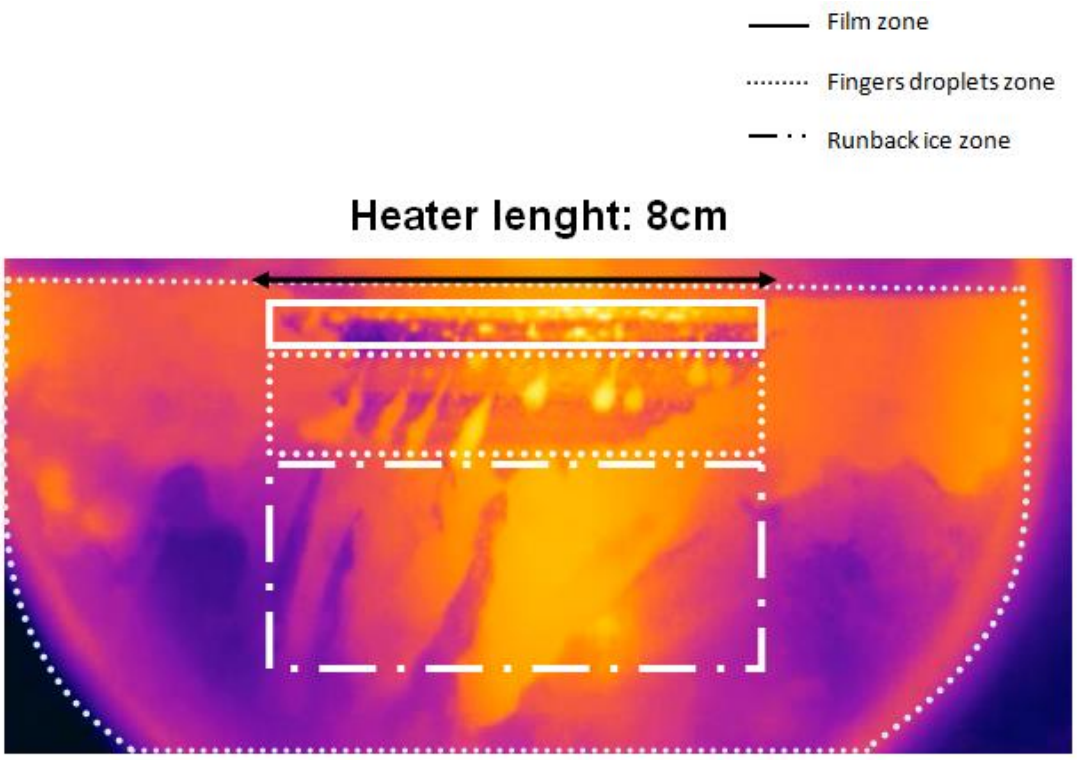

Fig. 4. Visualization of water and ice accretion on a hydrophilic sample (bare aluminum) after 90 s of testing. Top view of the airfoil (leading edge is at the top of the image). Tests were performed in dense spray conditions (see Table 1). The heater fixed inside the leading edge had a length of 8 cm.

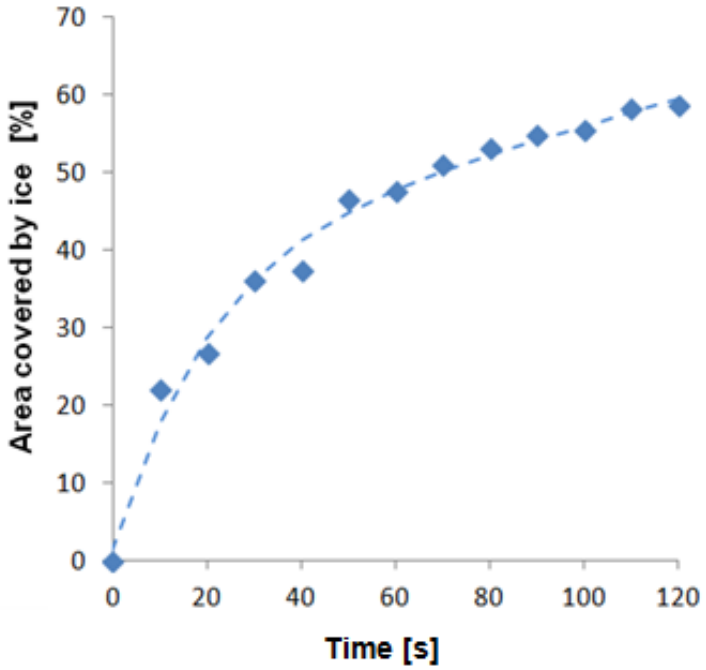

Fig. 5. Trend of the area covered by ice with respect the total area visible from the IR camera window, for the hydrophilic sample.

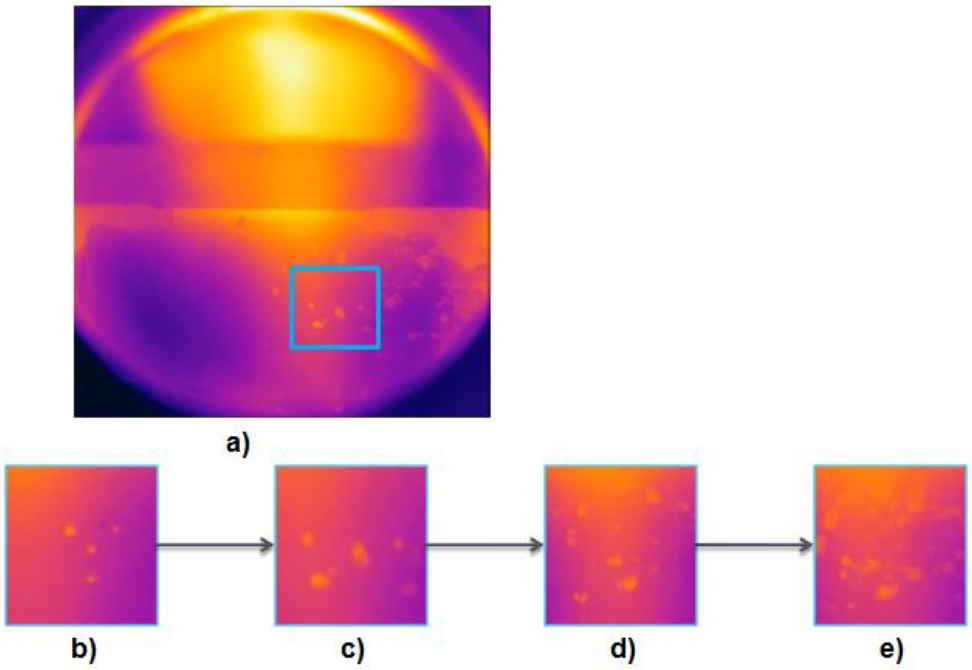

Fig. 6. a) Visualization of ice accretion on the superhydrophobic sample 50 s after the test started. Top view of the airfoil (leading edge is at the top of the image). (b), (c), (d), (e): represent a zoom-in view of the sample (blue box in (a)) after 30, 50, 70 and 110 s after test started, respectively. Tests were performed in dense spray conditions (see Table 2);

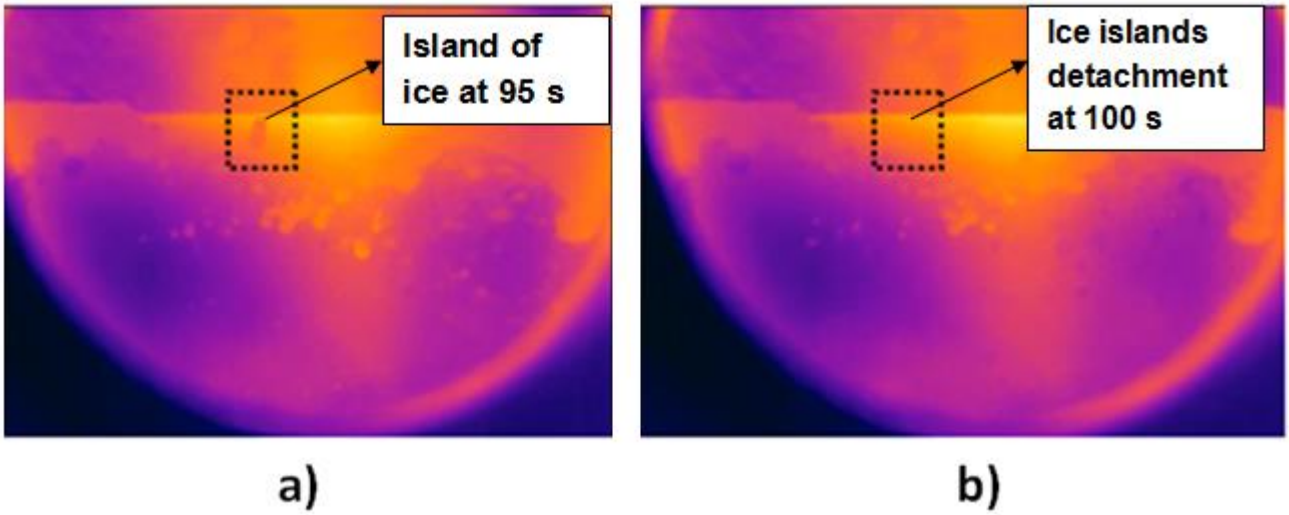

Fig. 7. Visualization of ice accretion on the superhydrophobic sample. Top view of the airfoil (leading edge is at the top of the image). Tests were performed in dense spray conditions (see Table 1). (a) shows image taken at 95 s; (b) shows image taken at 100 s. The ice island visible in the black rectangular section in (a) disappears in (b).

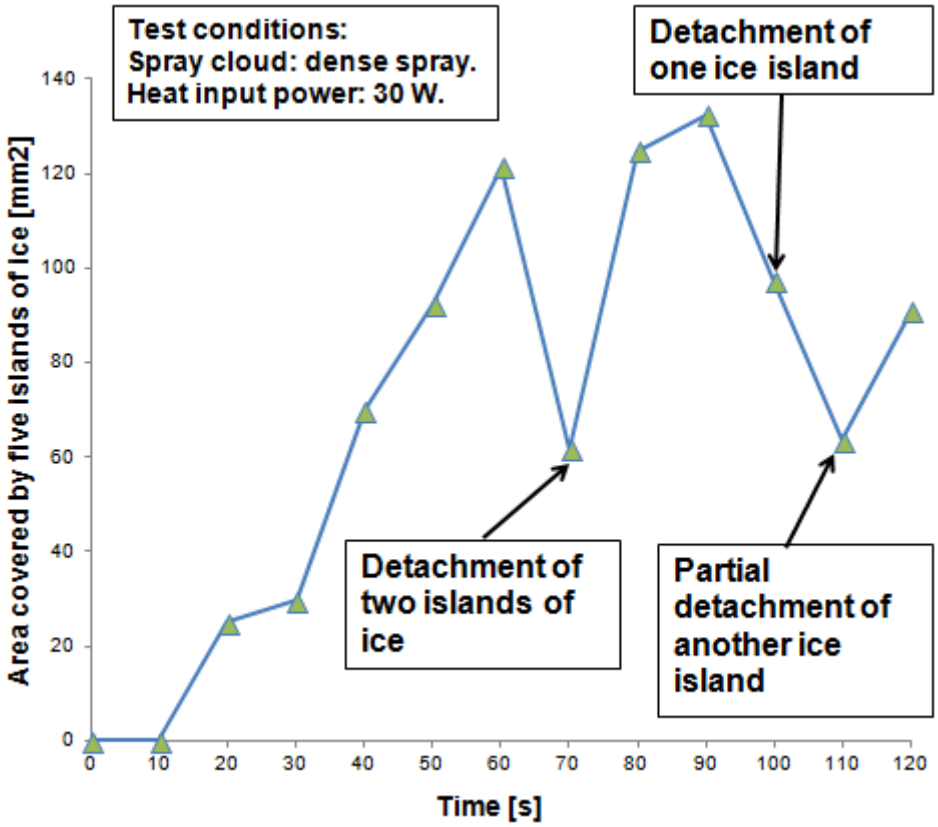

Fig. 8. The growth trend of the ice islands during the test. The trend is not monotonic because of the ice island detachment from the superhydrophobic surface. Two ice islands detached 70 s after the test started, and a third one detached at 100-110 s.

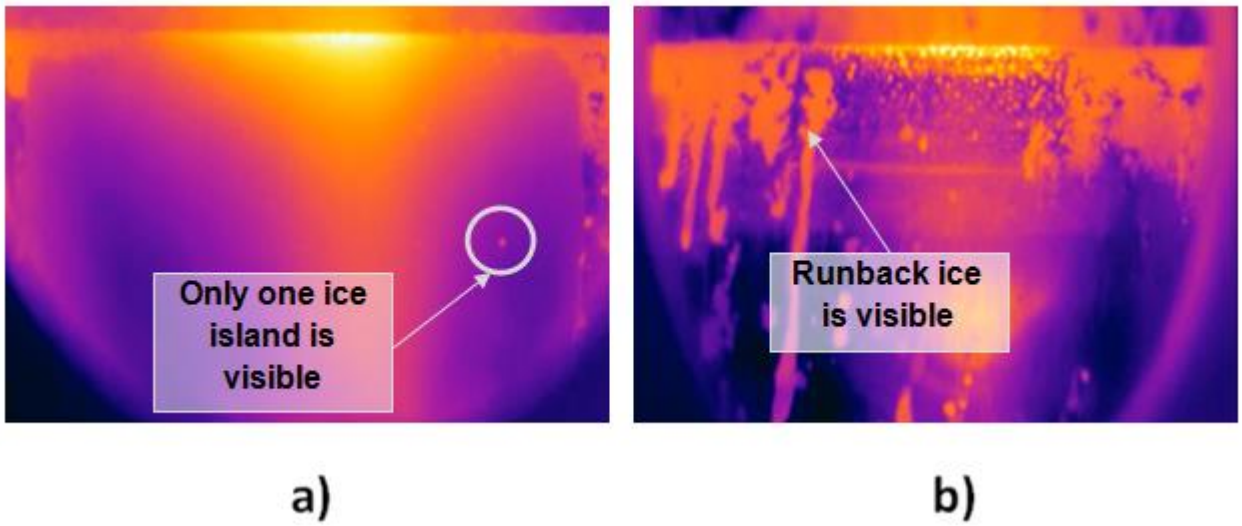

Fig. 9 (a) Image of the superhydrophobic surface 10 s after the test started. The sample appeared still ice-free, with the exception of one ice island. (b) Image of the hydrophilic surface 10 s after the test started. The runback ice covered ~20% of the sample area visible from the IR camera window.

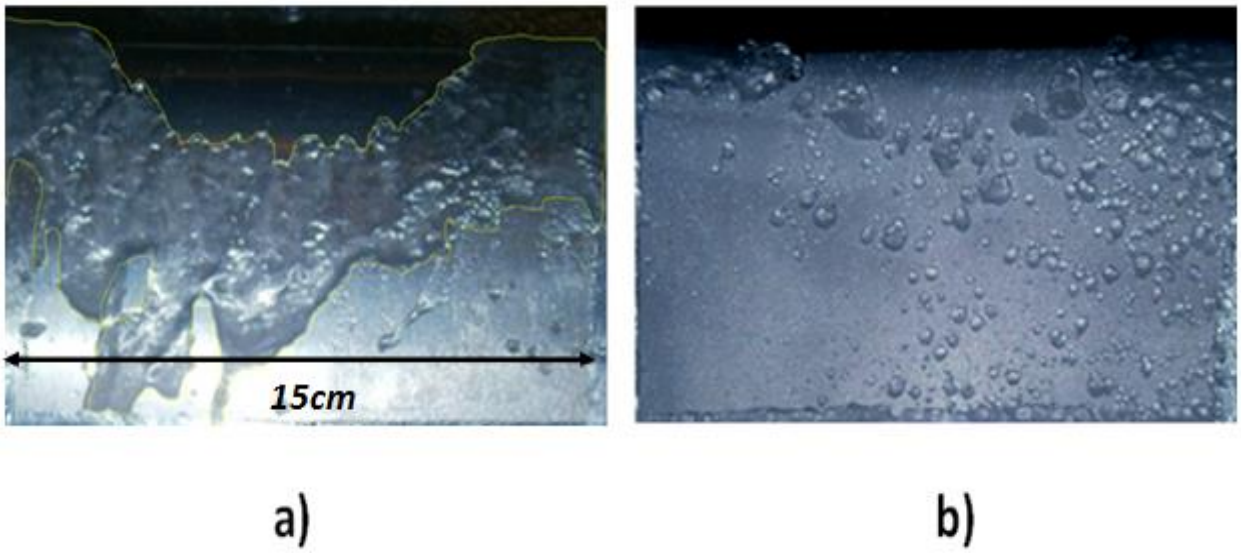

Fig. 10. Optical images taken at the end of the icing test, with dense spray conditions (see Table 1) and a heat input of 30 W: (a) hydrophilic sample (outline of ice covered area is highlighted), and (b) superhydrophobic sample.

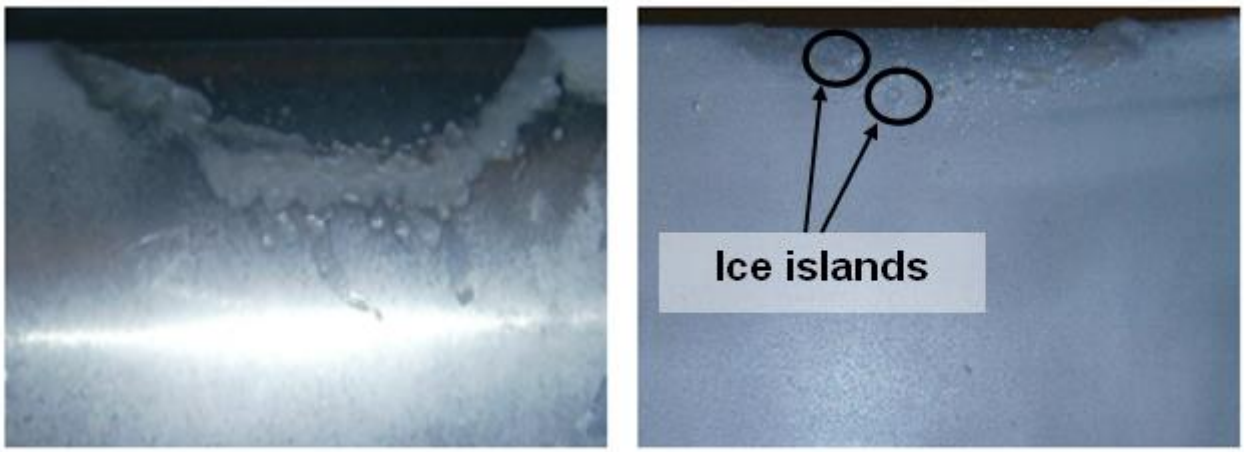

Fig. 11. Optical images taken at the end of the icing test, with disperse spray conditions (see Table 1): (a) hydrophilic sample (heat input 60 W), and (b) superhydrophobic sample (heat input 40 W). Ice accretion mechanisms is the similar as for the case with dense spray. Note that ice accretion is significantly less on superhydrophobic surface compared to the hydrophilic surface, despite the heat input being lower.

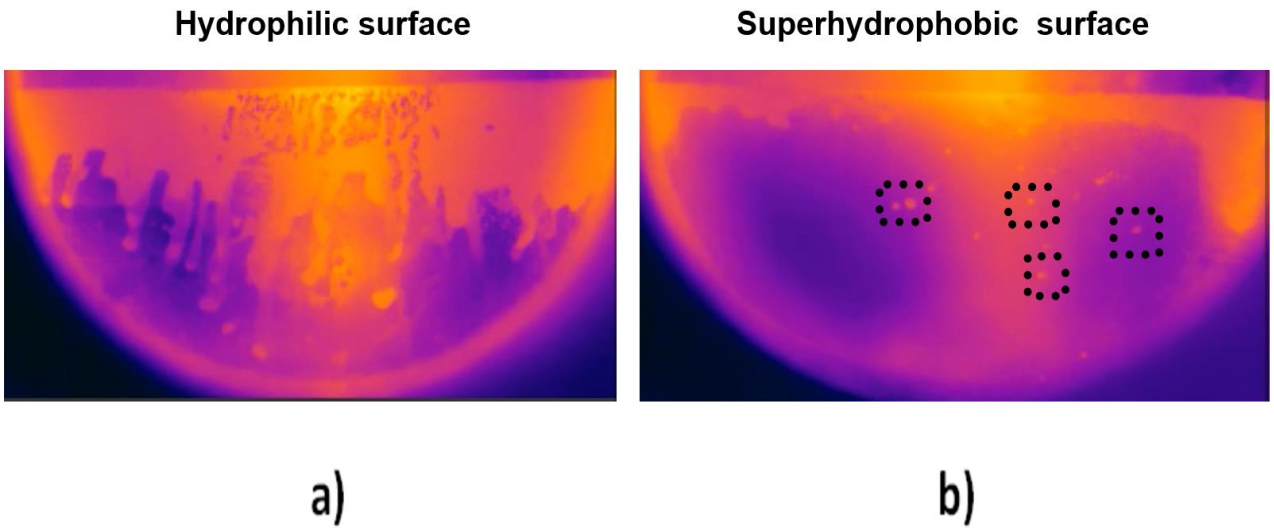

Fig. 12. IR camera visualization after 30 s of tests in dense spray conditions (see Table 1) and heat input of 18 W: (a) hydrophilic sample (runback ice is visible on the unheated zone of the sample), and (b) superhydrophobic sample, on which the ice islands are highlighted.

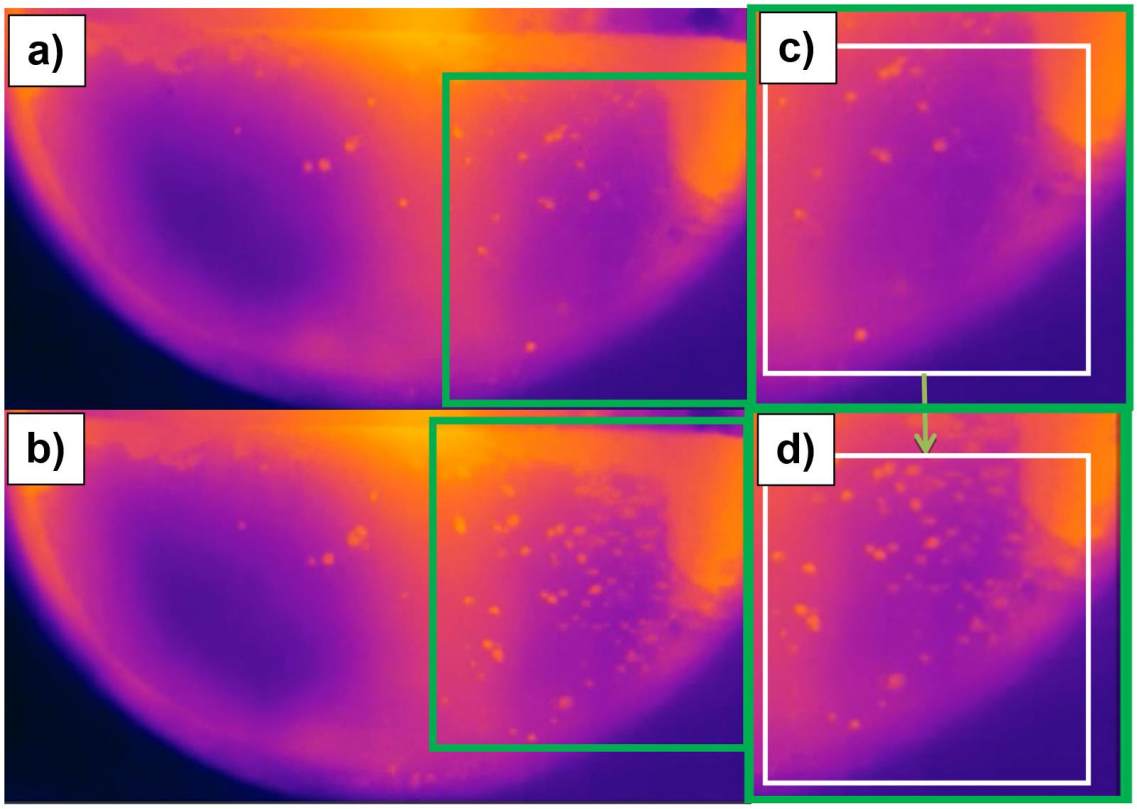

Fig. 13. Images taken from the IR camera during the test with dense spray conditions and heat input of 18 W on the superhydrophobic sample: (a) IR image at 26 s; (b) IR image at 27 s; (c) and (d) show a zoom-in view of the green boxes of the left column.

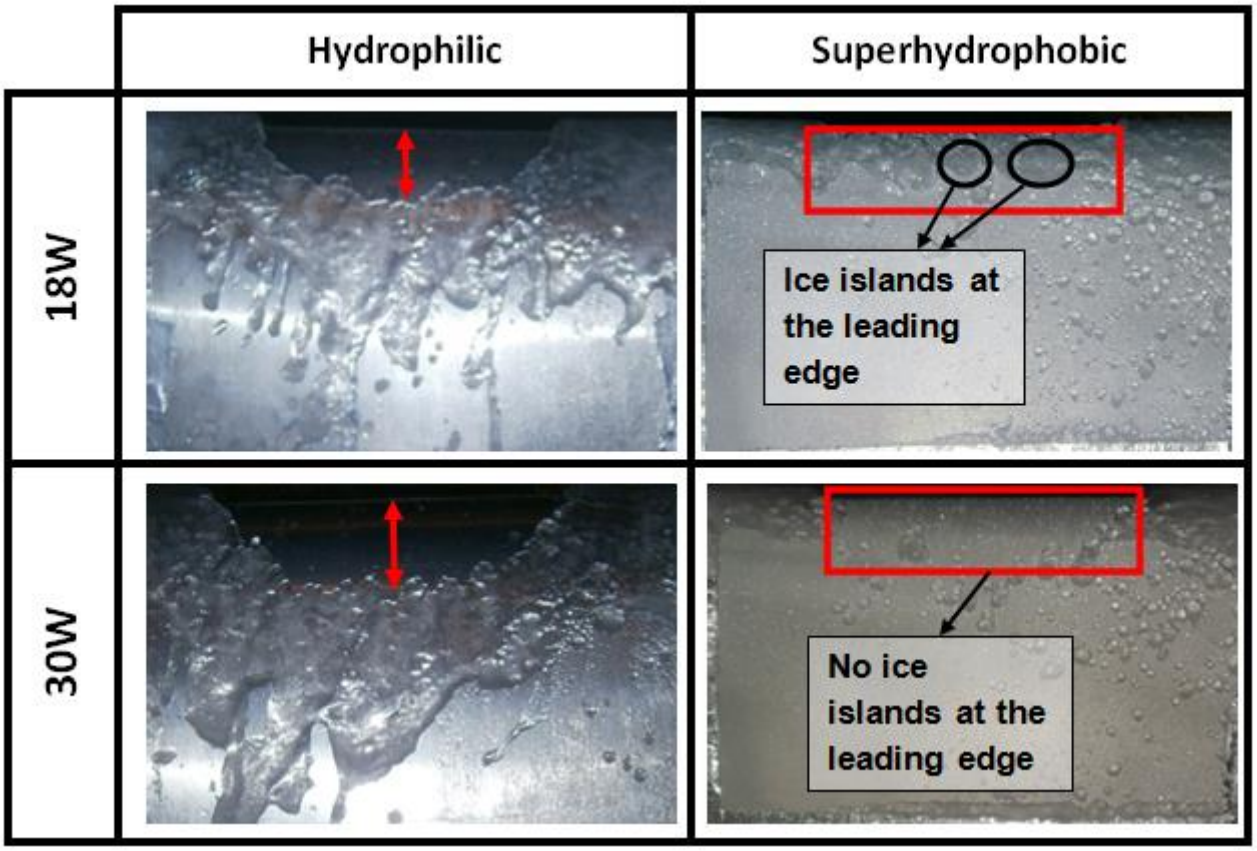

383

384 **Fig. 14.** Optical images taken at the end of the tests for both input heat power levels. The mechanisms
385 of ice accretion was the same for the 18 W and the 30 W cases: a compact front of ice for the
386 hydrophilic case and ice islands on the superhydrophobic surface. However, on the hydrophilic case
387 the runback ice started to accrete closer to the leading edge for the 18 W case (highlighted with red
388 arrows). On the superhydrophobic case, ice islands were visible closer to the leading edge for the
389 lowest input heat level tested (see red rectangular sections), as a result of a reduced heat input.